Physics of Fluids

Autoignition and detonation development induced by temperature gradient in n-C$_7$H$_{16}$/air/H$_2$O mixtures

Zhou Yu (于洲), **⬤ Huangwei Zhang** (张黄伟), **and Peng Dai** (戴鹏)

View Online   Export Citation   CrossMark

Physics of Fluids
GALLERY OF COVERS
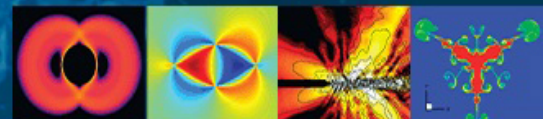
Autoignition and detonation development induced by temperature gradient in n-C$_7$H$_{16}$/air/H$_2$O mixtures

Zhou Yu, (于洲)[1] Huangwei Zhang, (张黄伟)[1,a] [iD] and Peng Dai (戴鹏)[2]

AFFILIATIONS

[1] Department of Mechanical Engineering, National University of Singapore, 9 Engineering Drive 1, Singapore 117576, Republic of Singapore

[2] Department of Mechanics and Aerospace Engineering, Southern University of Science and Technology, Shenzhen 518055, China

[a] Author to whom correspondence should be addressed: huangwei.zhang@nus.edu.sg. **Tel.:** +65 6516 2557

ABSTRACT

The effects of water vapor dilution on autoignition and detonation development induced by an ignition spot with thermal non-uniformity in an n-C$_7$H$_{16}$/air mixture are numerically investigated. Zero-dimensional homogeneous ignition under constant-volume conditions is studied first. It is found that excitation time increases, whereas total heat release decreases with a H$_2$O vapor mole fraction. Moreover, the role of H$_2$O vapor diluents as a third body considerably influences the critical temperature gradient. One-dimensional autoignition and detonation development caused by temperature gradients in ignition spots is then studied. Three different autoignition modes are identified: (I) supersonic deflagrative wave, (II) detonative wave, and (III) subsonic deflagrative wave. It is found that H$_2$O dilution has a slightly better performance on detonation suppression than CO$_2$ dilution. The chemistry–acoustics interactions during autoignition development are weakened when the H$_2$O mole fraction is increased. Besides, H$_2$O vapor dilution can delay the detonation initiation and reduce detonation intensity. Furthermore, typical autoignition processes induced by a hotspot and the chemical effects of water vapor diluent are discussed. It is seen that the chemical effects of H$_2$O dilution do not affect the lower limits of detonation development curves. Besides, the third body effect from the H$_2$O vapor diluent is important in suppressing the detonation development for the investigated ignition spot size. Finally, the effects of equivalence ratios and ignition spot sizes on the autoignition modes of n-C$_7$H$_{16}$/air/H$_2$O mixtures are studied. It is observed that the water vapor diluted mixtures with the fuel-lean condition are advantageous in inhibiting detonation from localized thermal non-uniformity.

Published under license by AIP Publishing. https://doi.org/10.1063/5.0038125

NOMENCLATURE

a	sound speed
E	total energy
h	total enthalpy
$\bar{M}$	mean molecular weight
P	pressure
q	the rate of progress variable
R	universal gas constant
t, r	temporal and spatial coordinates
T	temperature
u	flow velocity
X	mole fraction
Y	mass fraction

Greek letters

ξ	normalized temperature gradient
ε	normalized acoustic time
ξ_a	the ratio of sound speed to average reaction front propagation speed
τ	ignition delay time
τ_e	excitation time

ϕ	equivalence ratio
τ_1	viscous stresses
τ_2	viscous stresses
ρ	density
ω	production rate
μ	dynamic viscosity

Abbreviations

ICE	internal combustion engine
SIE	spark ignition engine
FVM	finite volume method
AMR	adaptive mesh refinement
NTC	negative temperature coefficient
0D	zero-dimensional
1D	one-dimensional

Subscripts

0	initial state
$i,0$	initial state outside spot
$r_0/2$	the middle of the ignition spot
c	critical value
n	total number of species
i	ith species
T	variable related to temperature
r	spatial coordinate
W	right boundary
u	upper
l	lower

superscripts

0	undiluted mixture

I. INTRODUCTION

Downsizing of spark ignition engines (SIEs) with turbocharging technology has been deemed to be a promising method since it can provide a novel solution for CO_2 reduction and fuel economy.[1] However, knocking combustion may occur under some unfavorable conditions and has become a stumbling block for SIEs with a high compression ratio.[2–6] It is known that the conventional knock is caused by end-gas autoignition, while the super-knock is associated with the interactions between the acoustic wave and the chemical reaction and detonation development.[1,7] In particular, autoignition and detonation development subject to localized reactivity non-uniformity (e.g., temperature non-uniformity) in the chamber is believed to play a dominant role in inducing this peculiar phenomenon.[8,9] A gaseous detonation consists of the interaction between the supersonic shock wave and the exothermic chemical reaction and, thus, propagates supersonically in a detonable medium.[10–12] How to suppress the super-knock induced by detonation arising from the non-uniform reactivity is an outstanding issue for performance improvement and technological innovation of SIEs.

Based on the pioneering work by Zeldovich,[13] different autoignition modes caused by a hotspot with thermal non-uniformity were identified, i.e., subsonic reaction wave, detonation development, and supersonic reaction wave. Grounded on this theory, numerous simulations considering simplified or detailed chemical mechanisms have been performed. A detonation peninsula, parameterized by two non-dimensional parameters related to the hotspot (normalized temperature gradient ξ and normalized acoustic time ε), was introduced by Bradley and his co-workers.[14–17] A quantitative description of different autoignition modes under engine-relevant conditions has been drawn in a ξ–ε diagram, and related studies were conducted for engine knock.[18–22] These studies mainly focused on identifying the modes of autoignition and reaction propagation in engines. From these studies, we can know that different autoignition regimes in engines (including thermal explosion, subsonic autoignition, detonation, and deflagration) can be identified and characterized by the ξ–ε diagram.

One-dimensional (1D) simulations were conducted to uncover the underpinning mechanism of autoignition and detonation development from a localized ignition spot.[23–37] For instance, Pan et al.[23] simulated the temperature gradient induced detonation development for three alternative C_{0-1} fuels (i.e., H_2, CH_4, and CH_3OH). The quantitative differences between different fuels were observable in terms of detonation development regime. In addition, Gao et al.[24] studied autoignition and detonation development in H_2/air mixtures. They pointed out that the thermodynamic conditions of mixture play an important role in detonation development. As for realistic fuels that may have low-temperature chemistry and a negative temperature coefficient (NTC) phenomenon, a cold spot may initiate the autoigniting flame front. Dai et al.[30–34] investigated the various effects on autoignition and detonation development in DME/air and n-C_7H_{16}/air mixtures under engine-relevant conditions. Both the cold spot and the hotspot were used to generate the autoignition reaction wave. Recently, Dai et al.[34] investigated autoignition and detonation development induced by a hotspot in fuel-lean and CO_2 diluted n-C_7H_{16}/air mixtures. The detonation development regimes for n-C_7H_{16}/air/CO_2 mixtures were identified. They found that the excitation time was a key factor in detonation development, and reducing an equivalence ratio had the same influence on the autoignition mode as increasing CO_2 dilution for the same excitation time. Terashima et al.[27–29] also performed 1D simulations to unveil the mechanisms of pressure wave development in end-gas autoignition during knocking combustion. They found that the amplitude of pressure oscillations was affected by low-temperature chemistry, and the strong pressure wave was induced by a hotspot with high reactivity.

High-resolution numerical simulations were also conducted to investigate the effects of temperature or composition inhomogeneities on autoignition and knock formation. For instance, Luong et al.[38,39] found that the fluctuations of temperature or composition were essential in inducing ignition of a lean n-C_7H_{16}/air mixture, and the super-knock intensity was significantly reduced by decreasing energetic length scale. Besides, Luong et al.[40] also introduced a new parameter (the statistical volume-averaged Sankaran number) and applied it to draw a newly developed ignition regime criterion for both NTC and non-NTC fuels successfully. Furthermore, Im et al.[41] performed a theoretical scaling analysis and extended the original Zel'dovich theory by combining characteristic Damköhler and Reynolds numbers in turbulent flows conditions. They pointed

out that the improved regime diagram was able to predict the ignition characteristics.

It is known that water injection technology is an effective approach to mitigate or alleviate knock in internal combustion engines.[42–44] This is because the injected water can effectively reduce the in-cylinder temperature because of high specific heat capacity and latent heat of vaporization of liquid water.[42,45] In addition, the water vapor acts as a diluent, leading to reduced pollutant emission, such as CO_2 and NO_x, and suppressing knocking combustion.[46,47] Although the water injection technology is popular, the underlying mechanism and performance in inhibiting detonation development due to localized reactivity non-uniformity under engine-relevant conditions are still not clear.[43,48,49] Recently, Zhuang et al.[50] studied hotspot induced autoignition and detonation characteristics of n-C_7H_{16}/air mixture laden with liquid water droplets. The effects of droplet diameter and number density on reactive front development were discussed in their work. However, the detonation development regime associated with the properties of the hotspot in water-containing mixtures is not studied therein.

In this study, detailed numerical simulations of autoignition and detonation development induced by the temperature gradient in water vapor diluted n-C_7H_{16}/air mixtures have been conducted. Our work aims at answering the following questions: (1) how does water vapor dilution (parameterized by mole fraction X_{H2O}) influence homogeneous n-C_7H_{16}/air autoignition? (2) How does X_{H2O} influence autoignition and detonation development from localized thermal non-uniformity? (3) What are the mechanisms of added water vapor in affecting auto-ignition reactive wave propagation? The rest of this article is structured as below. Section II introduces the mathematical and physical models used in this study. Zero-dimensional homogeneous ignition of n-C_7H_{16}/air/H_2O mixtures under the constant-volume condition is analyzed in Sec. III. One-dimensional autoignition and detonation development due to the ignition spot is studied in Sec. IV. Finally, Sec. V summarizes the main conclusions of this paper.

II. MATHEMATICAL AND PHYSICAL MODELS

The governing equations of momentum, energy, and species mass fraction equations are solved for one-dimensional, unsteady, multi-component, reacting flows. They can be written in a spherical coordinate as

$$\frac{\partial U}{\partial t} + \frac{\partial F(U)}{\partial r} + 2\frac{G(U)}{r} = F_v(U) + S_R, \qquad (1)$$

where t and r are time and radial coordinate, respectively. The third term at the left-hand side, $2G(U)/r$, is the geometry term. The vectors, $U, F(U), F_v(U), G(U)$, and S_R, respectively, have the following expressions:

$$U = \begin{pmatrix} \rho Y_1 \\ \rho Y_2 \\ . \\ . \\ . \\ \rho Y_n \\ \rho u \\ E \end{pmatrix}, F(U) = \begin{pmatrix} \rho u Y_1 \\ \rho u Y_2 \\ . \\ . \\ . \\ \rho u Y_n \\ \rho u^2 + P \\ (E+P)u \end{pmatrix}, G(U) = \begin{pmatrix} \rho u Y_1 \\ \rho u Y_2 \\ . \\ . \\ . \\ \rho u Y_n \\ \rho u^2 \\ (E+P)u \end{pmatrix},$$

$$\qquad (2)$$

$$F_v(U) = \begin{pmatrix} -r^{-2}(r^2 \rho Y_1 V_1')_r \\ -r^{-2}(r^2 \rho Y_2 V_2')_r \\ . \\ . \\ . \\ -r^{-2}(r^2 \rho Y_n V_n')_r \\ r^{-2}(r^2 \tau_1)_r - 2\tau_2/r \\ r^{-2}q_r + \Phi \end{pmatrix}, S_R = \begin{pmatrix} \omega_1 \\ \omega_2 \\ . \\ . \\ . \\ \omega_n \\ 0 \\ 0 \end{pmatrix},$$

where ρ is the density and u is the radial velocity. $E \equiv -P + \rho u^2/2 + \rho h$ is the total energy. h is the total enthalpy. P is the pressure, obtained from the ideal gas equation of state, i.e., $P = \rho R T/\bar{M}$, where R is the universal gas constant and $\bar{M}$ is the mixture molecular weight. Y_i and ω_i are the mass fraction and chemical reaction rate of ith species, respectively. n is the number of species. The diffusion velocity V_i' is determined using the mixture-averaged method. The chemical reaction rate ω_i is calculated by using the CHEMKIN package.[51] The thermodynamic and transport properties are evaluated using CHEMKIN and TRANSPORT packages.[51,52] Moreover, in Eq. (2), the symbol "$(\cdot)_r$" in the vector $F_v(U)$ stands for the partial derivative with respect to the spatial coordinate r. τ_1 and τ_2 are the viscous stresses, and q_r is the diffusive heat flux. Besides, Φ is the viscous dissipation rate. More details about the equations can be found in Refs. 34 and 53. Note that the continuity equation is not solved since it can be recovered through summing all the species mass fraction equations.

The governing equations [i.e., Eq. (1)] are solved using the in-house code A-SURF (Adaptive Simulation of Unsteady Reactive Flow),[54,55] which has been proven to be an accurate tool for predicting shock wave and transient autoignition process, based on numerous previous work.[24,30–34] Finite Volume Method (FVM) is adopted to discretize Eq. (1). The Strang splitting fractional-step procedure with second-order accuracy is used to separate the time evolution of reaction term S_R from that of the convection term $F(U)$ and diffusion term $F_v(U)$ to reduce the overall computational cost. In the first fractional step, the results of the non-reactive flow are obtained. During this step, the second-order accurate, Runge–Kutta, MUSCL–Hancock and central differencing schemes are used to discretize unsteady, convection and diffusion terms, respectively. In the second fractional step, the reaction term is integrated using the point implicit method. Moreover, a skeletal chemical mechanism for n-C_7H_{16} oxidation (44 species and 112 reactions[56]) is used in this work. It has been validated and successfully used in detonation simulations by Dai et al.[30,31,34] and Zhuang et al.[50]
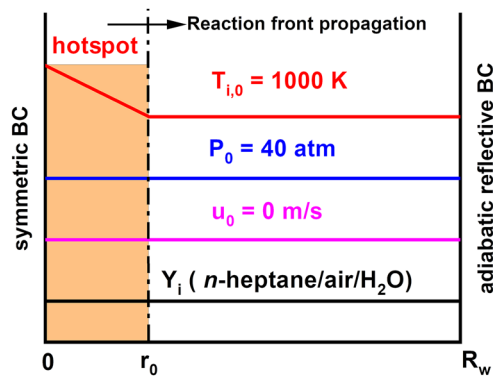
FIG. 1. Schematic of reactive wave propagation in the 1D spherical closed reactor.

The schematic of the 1D spherical closed reactor is shown in Fig. 1. The radius of the reactor is $R_W = 4$ cm. It is filled with spatially uniform n-C_7H_{16}/air/H_2O mixtures with various equivalence ratios. Furthermore, the mole fraction of water vapor ranges from 0 to 0.25. The distributions of the initial pressure and gas velocity are uniform in the domain, i.e., $P_0 = 40$ atm and $u_0 = 0$ m/s. In this work, the reactive front is initiated by a localized ignition spot with a constant temperature gradient near the left boundary, as shown in Fig. 1. Therefore, the initial temperature distribution T_0 in the reactor reads

$$T_0(r) = T(t=0, r) = \begin{cases} T_{i,0} + (r - r_0)\dfrac{dT_0}{dr}, & \text{for } 0 \le r \le r_0 \\ T_{i,0}, & \text{for } r_0 < r \le R_W, \end{cases}$$
(3)

where r_0 is the radius of the ignition spot. dT_0/dr is the temperature gradient inside the ignition spot and needs to be specified in our study. $T_{i,0}$ is the initial temperature beyond the spot. In this work, $T_{i,0} = 1000$ K and negative temperature gradients ($dT_0/dr < 0$) are considered, which correspond to a hotspot, as shown in Fig. 1. Here, P_0 and $T_{i,0}$ are chosen to mimic the high pressure and temperature conditions in the end gas of internal combustion engine chambers.

Symmetric boundary and adiabatic reflective condition are enforced at $r = 0$ and $r = R_W$, respectively. They correspond to the same conditions, i.e.,

$$u = 0, \quad \frac{\partial T}{\partial r} = \frac{\partial Y_i}{\partial r} = \frac{\partial P}{\partial r} = 0.$$
(4)

A multi-level, dynamically Adaptive Mesh Refinement (AMR) algorithm[57] is implemented in A-SURF to sufficiently resolve the characteristic aerodynamic or reactive fronts, e.g., detonation, pressure, and shock waves. In this study, the maximum level of refinement is 9, which leads to the finest cell of about 2.0 μm and the time step of 5×10^{-11} s. Mesh sensitivity has been performed (results not shown here), and it is found that the results are almost the same when the mesh size and/or time step are further reduced. Similar time and space resolutions are also used in the previous work with A-SURF in simulating autoignition and detonation wave propagation.[23,24,33,34]

III. ZERO-DIMENSIONAL HOMOGENEOUS IGNITION

Three parameters can be typically used for describing reaction front initiation by an ignition spot with temperature non-uniformity, i.e., ignition delay time, excitation time, and critical temperature gradient. Here, the ignition delay time τ and excitation time τ_e are estimated from zero-dimensional homogeneous ignition based on the representative thermochemical conditions in the ignition spot (e.g., in the middle of the spot). τ is defined as the time when the heat release rate reaches its peak in the homogeneous ignition process, while τ_e is the time interval from 5% to the maximum heat release rate.[15]

An autoignition wave may be initiated due to a distribution of initial temperature inside the ignition spot and hence local ignition delay time. The propagation speed of the autoignition wave, u_a, is inversely proportional to the gradient of ignition delay,[15] i.e.,

$$u_a = \left(\frac{d\tau}{dr}\right)^{-1} = \left(\frac{d\tau}{dT_0} \cdot \frac{dT_0}{dr}\right)^{-1}.$$
(5)

Based on the theories by Zel'dovich,[13] detonation development may occur due to the mutual reinforcement between the pressure wave and the local heat release, when the autoignition wave propagation speed equals the sound speed a. Therefore, the critical temperature gradient, $(dT_0/dr)_c$, is defined when $u_a = a$,[15]

$$\left(\frac{dT_0}{dr}\right)_c = \left(a\frac{d\tau}{dT_0}\right)^{-1},$$
(6)

where $a = \sqrt{kR_gT}$ is the sound speed and calculated with thermodynamic parameters from a characteristic location inside the ignition spot. Here, k is the adiabatic index and R_g is the gas constant. In this section, the foregoing parameters will be analyzed based on 0D homogeneous ignition calculations.

Zero-dimensional homogeneous ignition of n-C_7H_{16}/air/H_2O mixtures under the constant-volume condition is calculated, and Fig. 2 shows the ignition delay time, excitation time, and the critical temperature gradient of n-C_7H_{16}/air/H_2O mixtures with different initial temperatures and H_2O mole fractions. It is seen that for the water-free stoichiometric mixture ($X_{H_2O} = 0$), NTC dependence of ignition delay time on the initial temperature is observed between about 850 K and 950 K. When the mixture equivalence ratio is $\phi = 1$, increasing the H_2O mole fraction to 0.1 and 0.2 has a negligible influence on the NTC temperature range. However, the non-monotonicity of ignition delay time becomes less pronounced with a higher H_2O mole fraction for the stoichiometric mixture. This indicates that the NTC phenomenon is weakened with H_2O dilution. For low and intermediate temperatures ($T_0 < 950$ K), the ignition delay time τ first decreases with X_{H_2O} and then increases, but generally, the changes in τ are still limited. When the H_2O mole fraction is fixed (e.g., $X_{H_2O} = 0.2$), the ignition delay time increases for the lean mixtures.

It can be observed from Fig. 2(b) that the excitation time τ_e is much smaller than the ignition delay time τ. Moreover, τ_e monotonically decreases (increases) with the initial temperature (H_2O mole fraction). When the mixture composition deviates from the stoichiometric conditions, the excitation time τ_e increases considerably, which is particularly true for fuel-lean mixtures, as shown in Fig. 2(b). Because of the NTC effects, the distributions of the critical
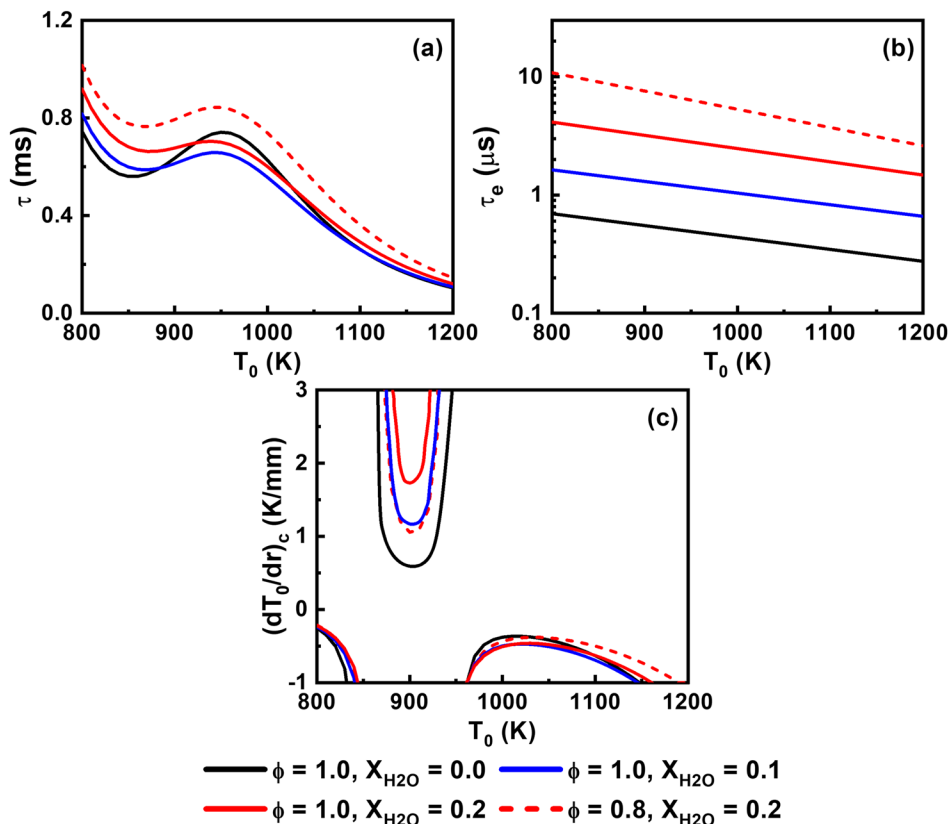
FIG. 2. (a) Ignition delay time, (b) excitation time, and (c) the critical temperature gradient of n-C_7H_{16}/air/H_2O mixtures as functions of initial temperature. Initial pressure is 40 atm.

temperature gradient have three separate sections [see Fig. 2(c)]. For the stoichiometric mixtures, the critical temperature gradients at $T_0 = 1000$ K have minor differences.

In order to unveil the thermal and chemical kinetic effects of H_2O dilution on the ignition characteristics, Fig. 3 plots the change in ignition delay time, excitation time, and the critical temperature gradient of n-C_7H_{16}/air/H_2O mixtures with different diluents. The
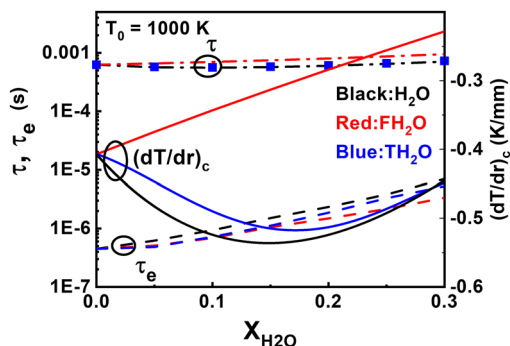
FIG. 3. Change in ignition delay time, excitation time, and the critical temperature gradient of n-C_7H_{16}/air/H_2O mixtures with different diluents (H_2O, FH_2O, and TH_2O). The initial temperature is 1000 K.

initial temperature is fixed to be $T_0 = 1000$ K. Following the work of Zhang *et al.*,[58] two hypothetical species are used to denote the water vapor diluents, i.e., FH_2O and TH_2O, which share the same thermophysical properties as real H_2O species. Here, FH_2O denotes chemically inert H_2O species (not act as the reactant or third body in elementary reactions), while TH_2O is a water species acting as a third body only. The third body coefficients of TH_2O are the same as those of real H_2O. Observation of Fig. 3 reveals that FH_2O leads to slightly higher ignition delay time and lower excitation time relative to the results of real H_2O. However, the critical temperature gradient monotonically increases with FH_2O mole fractions. This is different from that with real H_2O species, for which non-monotonic variations are observed with the diluent mole fraction. This indicates that H_2O vapor as the reactant and/or third body considerably influences the critical temperature gradient. The role of water species as a third body can be confirmed through the results of TH_2O dilution, which are generally closer to the real H_2O results. This implies that the effects of water species as a third body are more important than as reactants. This finding can also be corroborated by the different results with FH_2O and TH_2O, particularly for the critical temperature gradient.

The effects of H_2O vapor addition in n-C_7H_{16}/air mixtures on elementary reactions are investigated based on sensitivity analysis.[59–61] Here, the sensitivity coefficient is defined as $(\tau(2A) - \tau(A))/\tau(A)$, where A is the pre-exponential factor of the selected reaction. A positive (negative) value of the selected

elementary reaction indicates that it suppresses (promotes) the autoignition process. Meanwhile, reactions having higher magnitude of sensitivity coefficient are deemed the reactions with larger contribution toward the ignition delay time. Figure 4 shows the elementary reactions with the highest sensitivity coefficients with different H_2O initial molar fractions. For the stoichiometric mixtures with the H_2O molar faction from $X_{H_2O} = 0$ to $X_{H_2O} = 0.15$, both R107 ($PC_7H_{15}O_2 => PHEOOHX_2$, i.e., $RO_2 => QOOH$) and R102 ($NXC_7H_{16} + HO_2 => SXC_7H_{15} + H_2O_2$, i.e., $RH + HO_2 => R + H_2O_2$) are important. R107 and R102 can be treated as the major reactions for the n-C_7H_{16} oxidation. As we can see, H_2O acts as a product in R13 ($HO_2 + OH <=> H_2O + O_2$). Therefore, as the mixtures are diluted with more water vapor, R13 becomes more important. This explains why the ignition delay time increases for the mixtures with the higher H_2O mole fraction. Besides, H_2O also acts as a third body in R15 ($2OH + M <=> H_2O_2 + M$), and R15 is expected to facilitate autoignition.

Moreover, the effects of H_2O dilution on total heat release are shown in Fig. 5. The relations between total heat release, excitation time, and the mole fraction of H_2O are elaborated here. The total heat release is the time integrated heat release rate during the homogeneous ignition process. The latter is $\omega_T = -\sum_{i=1}^{n} \Delta h_{f,i}^0 \omega_i$, with $\Delta h_{f,i}^0$ and ω_i being the chemical enthalpy and reaction rate of ith species, respectively. The specific chemical enthalpy of H_2O is about $-13\,435$ kJ/kg.[62] Thus, regardless of the effects of H_2O dilution on the reaction pathway, the total heat release decreases with the H_2O mole fraction. Besides, one can see from Fig. 3 that the higher mole fraction of H_2O corresponds to lager excitation time. Therefore, the total heat release decreases with the excitation time. These are confirmed in Fig. 5, which shows that the total heat release decreases with the H_2O mole fraction or excitation time for both stoichiometric and lean n-C_7H_{16}/air/H_2O mixtures.

IV. ONE-DIMENSIONAL AUTOIGNITION WITH TEMPERATURE NON-UNIFORMITY

Autoignition reaction front development induced by an ignition spot with the temperature gradient will be studied in this section with one-dimensional simulations. It is known that the resonance
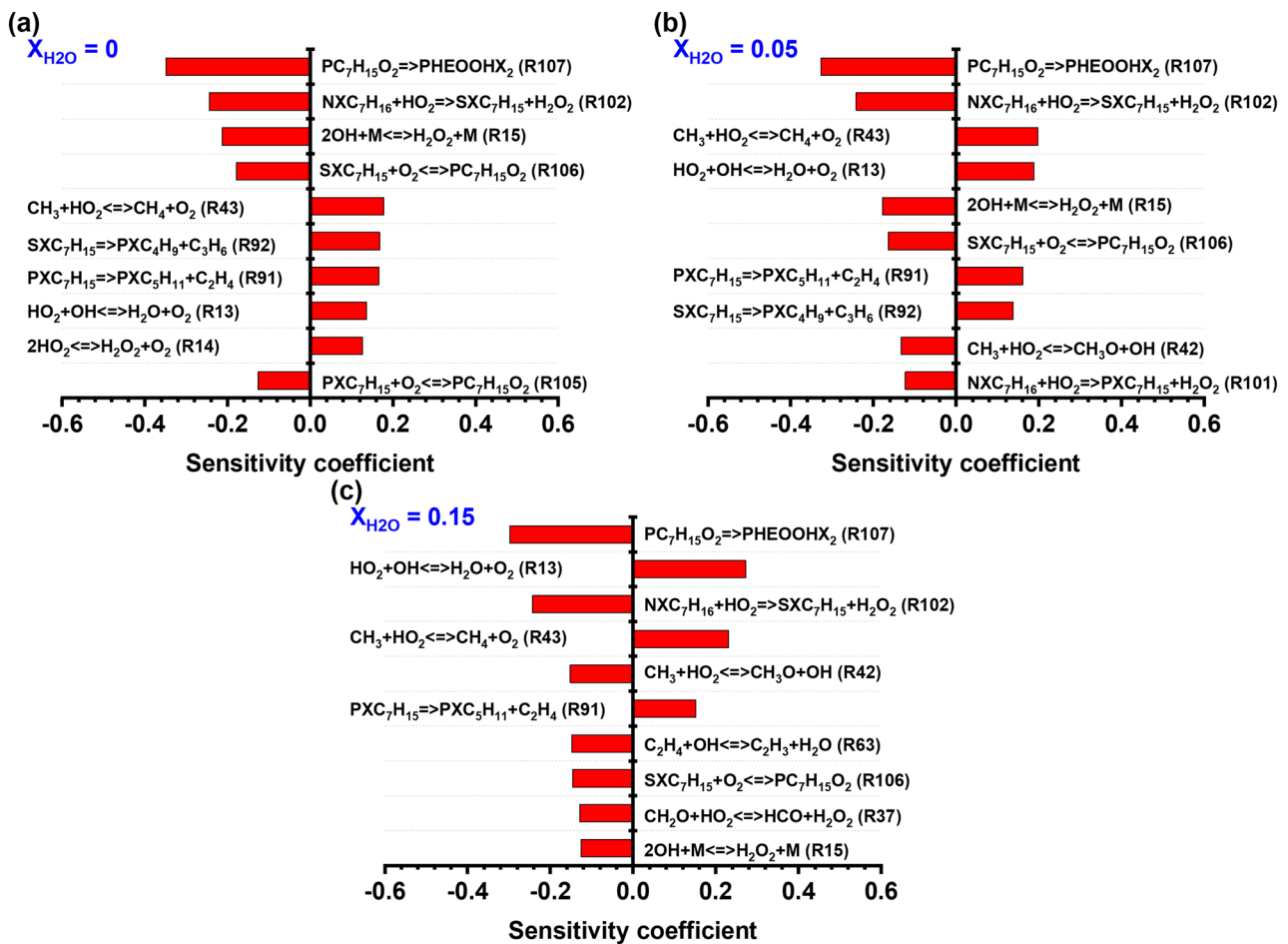
FIG. 4. Elementary reactions with the highest sensitivity coefficients under different initial H_2O molar fractions: (a) 0, (b) 0.05, and (c) 0.15. The initial temperature is 1000 K.
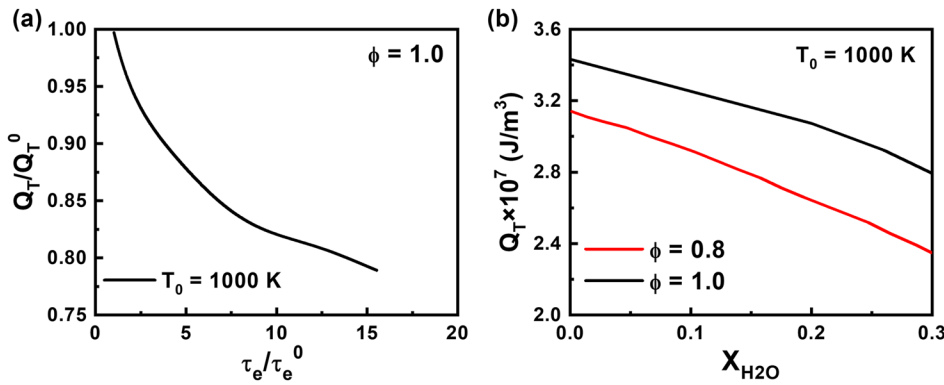
FIG. 5. Total heat release as a function of (a) excitation time and (b) H_2O mole fraction. Q_T^0 and τ_e^0 are total heat release and excitation time of undiluted stoichiometric mixtures, respectively.

between the autoignition wave and the acoustic wave plays a critical role in detonation development.[13,15] The couplings of these two waves can be categorized by *acoustic-induction coupling* and *acoustic-exothermicity coupling*, respectively.[63] The former is quantified by the normalized temperature gradient ξ, while the latter is quantified by the ratio (denoted with ε) of characteristic timescale for the chemical heat release to residence time for the acoustic wave inside the ignition spot.[14,15]

The normalized temperature gradient ξ is defined as the ratio of sound speed a (middle of the ignition spot in this work) to autoignition reaction front propagation speed u_a,

$$\xi = \frac{a_{r_0/2}}{u_a} = \frac{a_{r_0/2}}{dr/d\tau}. \tag{7}$$

With Eq. (5), Eq. (7) can be further written as

$$\xi = \frac{dT_0/dr}{(dT_0/dr)_{c,r_0/2}}, \tag{8}$$

where dT_0/dr is the initial temperature gradient within the ignition spot [see Eq. (3)], whereas $(dT_0/dr)_{c,r_0/2}$ is the critical temperature gradient. The subscript "$r_0/2$" indicates that the quantity is estimated based on the initial thermochemical properties in the middle of the ignition spot. Therefore, the autoignition reaction front propagation speed reads

$$u_a = a_{r_0/2}/\xi. \tag{9}$$

However, the estimation from Eq. (9) is usually not equal to the real propagation speed. This is mainly due to the variations of species and thermal diffusions inside the ignition spot during the induction period. Instead, the average propagation speed S_{AVG} of the reaction front in the ignition spot from one-dimensional simulations will be used to calculate the normalized temperature gradient,[33,34]

$$\xi_a = a_{r_0/2}/S_{AVG}. \tag{10}$$

The second parameter, ε, measures the time scale of reaction heat release relative to the propagation time of the acoustic wave in the ignition spot. Therefore, it is defined as

$$\varepsilon = \frac{r_0/a_{r_0/2}}{\tau_e}. \tag{11}$$

Here, τ_e is from 0D calculations based on the properties at the middle of the ignition spot.

A. Autoignition in stoichiometric n-C$_7$H$_{16}$/air/H$_2$O mixtures induced by a hotspot

The autoignition modes of stoichiometric n-C$_7$H$_{16}$/air/H$_2$O mixtures due to the temperature gradient in a hotspot (i.e., $T_{i,0}$ = 1000 K) are shown in Fig. 6. The spot radius is r_0 = 3.5 mm. It is seen that for small and intermediate H$_2$O mole fractions X_{H2O}, the autoignition waves triggered by an ignition spot can fall into three categories: (I) supersonic deflagrative wave, i.e., an autoignitive deflagration propagating supersonically, (II) detonative wave with high maximum pressure (P_{max}/P_e, with P_{max} and P_e being the maximum pressure from 1D calculations and equilibrium pressure from 0D constant-volume autoignition calculations. This normalization can exclude the effect of total heat release[34]), and (III) subsonic deflagrative wave, i.e., a conventional deflagration propagating by molecular diffusion and convention.[15] The detonation development curve is mirrored *C*-shaped, with upper and lower limits (denoted with $\xi_{a,u}$ and $\xi_{a,l}$), respectively. When the H$_2$O mole fraction is higher than a critical value, detonation development from the ignition spot cannot be observed; instead, only supersonic (subsonic) deflagrative waves are present when the values of ξ_a are small (large). This is because the conditions required to enable coupling of acoustic waves with energy release cannot be achieved. The critical X_{H2O} in Fig. 6 is about 0.15 at r_0 = 3.5 mm.

Figure 7 shows the autoignition modes of stoichiometric n-C$_7$H$_{16}$/air/H$_2$O mixtures with r_0 = 3.5 mm in $\xi_a - \tau_e/\tau_e^0$ and $\xi_a - \varepsilon$ space, respectively. τ_e^0 is the excitation time of undiluted ($X_{H2O} = 0$) mixtures. Note that the excitation time ratio, τ_e/τ_e^0, and ε become larger and smaller, respectively, when the H$_2$O mole fraction is increased (see Fig. 3). Note that each excitation time corresponds to a H$_2$O mole fraction. In Fig. 7(a), the detonation development curve is a mirrored *C*-shaped curve, while it is *C*-shaped in Fig. 7(b). Same as in Fig. 6, three categories can be also observed in these two diagrams. The detonation development curves of stoichiometric n-C$_7$H$_{16}$/air/CO$_2$ mixtures[34] are also shown in Fig. 7. It is found that the effects of CO$_2$ and H$_2$O dilutions on autoignition modes are close. However, the regions of detonation development with H$_2$O dilution are slightly smaller than those with CO$_2$ dilution, with lower $\xi_{a,u}$ and higher $\xi_{a,l}$, respectively, as shown in Figs. 7(a) and 7(b). This indicates that H$_2$O dilution has a slightly better performance
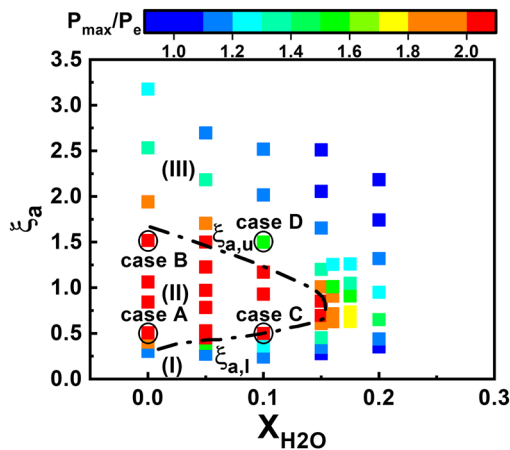
FIG. 6. Autoignition modes of stoichiometric n-C_7H_{16}/air/H_2O mixtures with different H_2O mole fractions. Ignition spot size is $r_0 = 3.5$ mm. Three categories are as follows: (I): supersonic deflagrative wave, (II): detonative wave, and (III): subsonic deflagrative wave.

FIG. 8. Change in normalized maximum pressure with normalized excitation time. Ignition spot radius is $r_0 = 3.5$ mm. The symbols along the x axis indicate the critical values of τ_e/τ_e^0 for each ξ_a.

in suppressing detonation development induced by thermal non-uniformity. It should be mentioned that these comparisons are made in terms of the mole fraction, although the heat capacities of the two diluents are different.

Furthermore, to demonstrate the effects of excitation time on autoignition characteristics, Fig. 8 shows the change in normalized maximum pressure P_{max}/P_e with normalized excitation time τ_e/τ_e^0 for stoichiometric n-C_7H_{16}/air mixtures with different levels of H_2O dilution. Three normalized temperature gradients are selected, i.e., $\xi_a = 0.5$, 1.0, and 1.5. The symbols along the x axis are the critical τ_e/τ_e^0 along the detonation development curve for each ξ_a, which are extracted from Fig. 7. No detonation occurs when τ_e/τ_e^0 is larger than its critical value. For a fixed ξ_a, P_{max}/P_e decreases when the normalized excitation time increases. This indicates that the peak pressures when autoignition and detonation evolves are lowered when the H_2O vapor mole fraction is increased. Among the three temperature gradients in Fig. 8, P_{max}/P_e with $\xi_a = 1.0$ is highest, due to the intensive interactions between the reaction wave and the acoustic wave during the autoignition process. Moreover, all three normalized maximum pressures are close when $\tau_e/\tau_e^0 > 5$, as no detonation occurs.

B. Typical autoignition process induced by a hotspot

In order to highlight the effects of the normalized temperature gradient and H_2O mole fraction on autoignition modes, four typical cases, i.e., cases A to D, are selected for further analysis. Their parameters are summarized in Table I. Cases A/B and C/D are chosen to reveal the effects of normalized temperature gradient. Besides, cases A/C and B/D are used to clarify the effects of H_2O mole fraction. These cases are also marked in Fig. 6. Note that in cases A/B/C, detonation development is observed, while in case D, only subsonic deflagrative wave is present. To obtain ξ_a in Table I, we calculate $a_{r_0/2}$ with different H_2O mole fractions based on 0D calculations and then estimate the corresponding S_{AVG} from 1D simulation considering various temperature gradients inside the ignition spot.

Figure 9 shows the temporal evolutions of pressure, temperature, and heat release rate distributions for cases A–D. It is seen from Fig. 9(a) that detonation wave is initiated inside the hotspot (i.e., $r_0/r < 1$) for case A (line No. 2), which has a relatively low normalized temperature gradient. However, for case B, the detonation wave develops outside the hotspot (i.e., $r_0/r > 1$) (line No. 3). This is because the average speed of autoignition front propagating within the ignition spot in case B is relatively low. Therefore, more time and longer distance are required for the reaction and pressure waves to
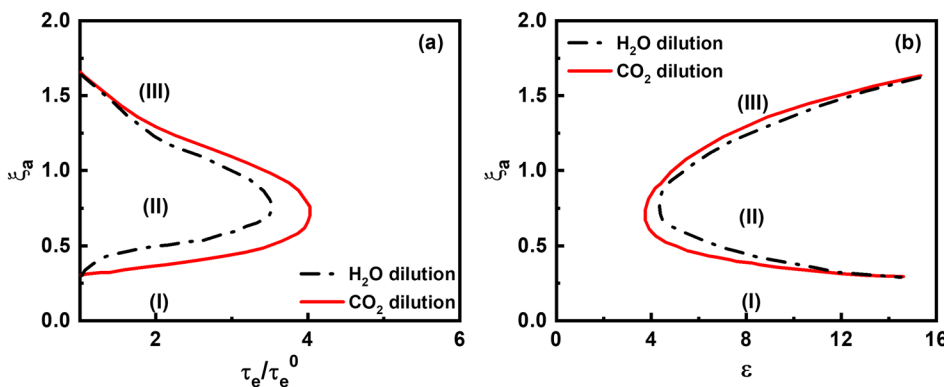
FIG. 7. Autoignition modes of stoichiometric n-C_7H_{16}/air/H_2O mixtures in (a) $\xi_a - \tau_e/\tau_e^0$ and (b) $\xi_a - \varepsilon$ space. Ignition spot radius is $r_0 = 3.5$ mm. The curves with CO_2 dilution are from Ref. 34. Implications for (I)–(III) are the same as in Fig. 6.

TABLE I. Parameters of four typical autoignition cases.

Case	X_{H_2O}	ξ_a	Mode
A	0	0.5	Detonation development
B	0	1.5	Detonation development
C	0.1	0.5	Detonation development
D	0.1	1.5	Subsonic deflagrative wave

mutually be enhanced and eventually be coupled, leading to a detonation wave. For these two cases, the detonation wave travels to the unburned mixtures (lines No. 2 to No. 5 in case A and No. 3 to No. 5 in case B) and is finally weakened by thermal explosion ahead of it (line No. 6), with the pressure close to P_e. Seen from Figs. 9(b) and 9(c), the temperature at the flame front and the maximum heat release rate become high when detonation happens (e.g., line No. 3 in two cases).

Furthermore, cases A and C are compared for the effects of H_2O diluent concentration in the detonable mixture with $\xi_a = 0.5$. With H_2O addition in case C, the maximum pressure decreases, which is consistent with the results shown in Fig. 8. The detonation onset location in case C (line No. 3) is around the right edge of the ignition spot, thereby farther away from the left boundary than that of case A (line No. 2). Besides, the detonation propagation distance in case C is shorter than in case A. This indicates that H_2O dilution can delay the detonation initiation and reduce detonation intensity. In cases B and D with the higher temperature gradient $\xi_a = 1.5$, no detonation occurs when H_2O is added in case D. Conversely, almost constant-pressure combustion occurs at the early stage, which can be confirmed by the nearly uniform pressure distribution (see lines No. 1 to No. 3). Besides, the maximum heat release rate is shown to continuously increase, which is accompanied by the continuously increased temperature of the unburnt gas due to the compression. Moreover, the maximum pressure of case D is only almost two thirds of that of case B.

Figure 10 shows the reaction front propagation speed in cases A to D. The reaction front location is defined as the location with
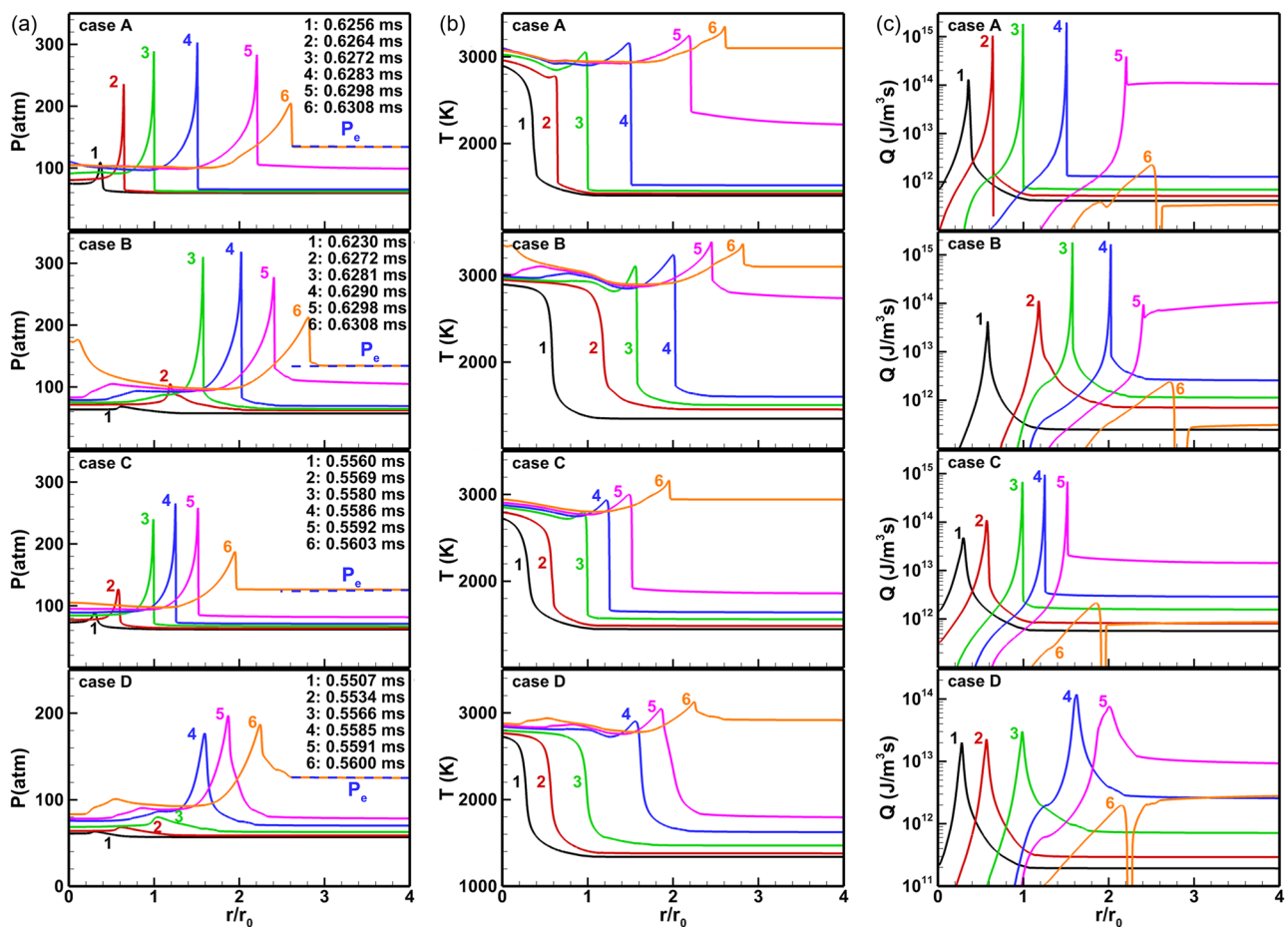
FIG. 9. Temporal evolutions of (a) pressure, (b) temperature, and (c) heat release rate during autoignition from a hotspot in cases A to D. The equilibrium pressure is P_e = 134 atm in cases A/B, while 125 atm in cases C/D.
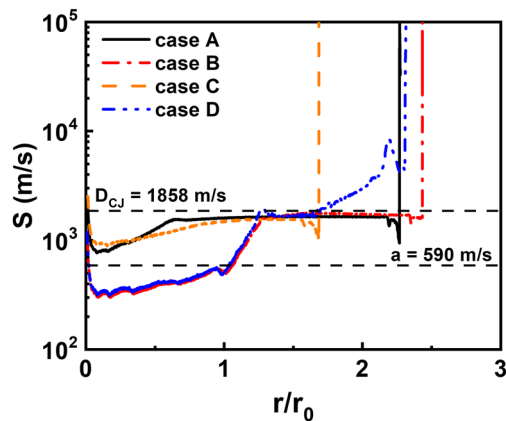
FIG. 10. Reaction front propagation speed, S, as a function of normalized position, r/r_0, in cases A to D. D_{CJ} is the Chapman–Jouguet speed, and a is the sound speed.

the maximum heat release rate. As shown in Fig. 10, the reaction front within the hotspot in cases A and C first propagates supersonically and then accelerates to the speeds close to the C–J speed. It is noted that the predicted wave speed is slightly lower than the C–J detonation wave speed. That is because the curvature effects from the spherical geometry considered here[64,65] and/or the end gas have partially reacted before the arrival of the detonation wave. Obviously, the reaction front propagation speed within the hotspot for case C is lower than that for case A, while the reaction front for cases B and D first propagates subsonically within the hotspot and then accelerates rapidly to a supersonic state around the edge of the hotspot. The acceleration is caused by the thermal explosion of the unburned mixture. Besides, the two curves of cases B and D overlap within the hotspot, which indicates that H_2O dilution has a negligible influence on the reaction front propagation within the hotspot at $\xi_a = 1.5$. Moreover, the reaction front of all four cases accelerates abruptly when the autoignition of mixture near the right boundary occurs (e.g., $r/r_0 \approx 2.3$ in case A).

In order to analyze the interactions between the chemical reaction and the pressure wave, Fig. 11 shows the evolution of thermal states of a particle initially at the right edge of the hotspot (i.e., $r = r_0 = 3.5$ mm) in cases A and B. The position of the particle is updated at each time step, through integrating the particle momentum equation. The thermal states of the Lagrangian particle are obtained from linear extrapolation of its two neighboring grids after its position is updated.[31,66] It is shown that the remarkable difference between the two cases is whether the detonation has developed or not when the pressure wave passes the specified particle [also see Fig. 9(a)]. In case A, the fluid in the particle undergoes an isochoric combustion during the initial stage (i.e., the part before point a on each curve). Then, the particle is compressed intensively when the pressure wave formed by the temperature gradient arrives (i.e., part ab on each curve). The specific volume at point b is almost half of that at point a. Meanwhile, the heat release rate increases rapidly and reaches its maximum value (i.e., point b along the Q–t curve) after this period. This leads to an enhanced interaction between the reaction wave and the pressure wave. After that, the pressure and heat release rate decrease significantly as gas expansion occurs (i.e., the
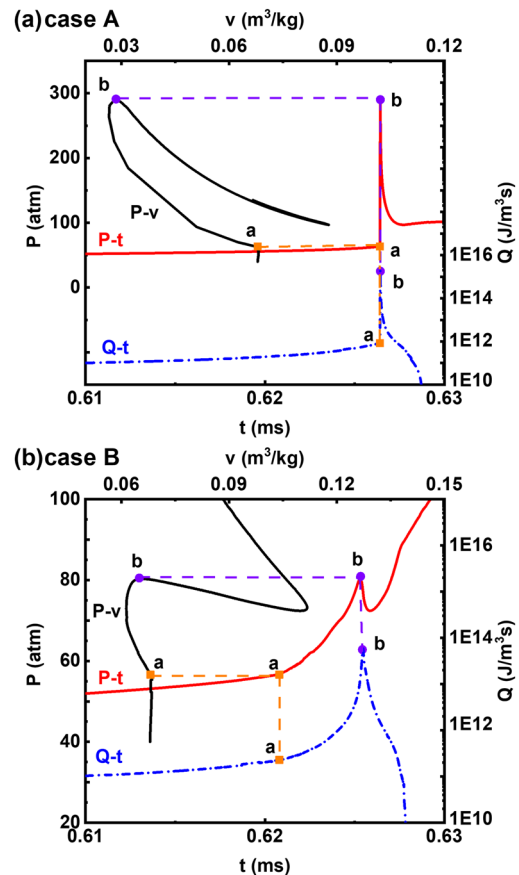
FIG. 11. Evolution of thermal states of a fluid particle initially at $r = r_0$ in cases (a) A and (b) B.

part after point b on each curve). In case B, similar evolution of thermal states during autoignition (i.e., the part before point b along each curve) can be observed. It is noted that detonation has not developed when the pressure wave passes the particle. Therefore, only a moderate interaction between the chemical reaction and the pressure wave takes place.

Figure 12 compares the P–v curves of the particle in cases A to D. It is noted that the compression effect caused by the pressure wave in case A is the strongest among the four cases, and accordingly, the largest pressure rise can be observed. With H_2O addition, the compression effect becomes weaker in case C, indicating that H_2O dilution can weaken the detonation development. As for cases B and D, it is known that these two cases correspond to different autoignition modes. The pressure rise of case B is slightly larger than that of case D. This demonstrates that the evolution of thermal states within the hotspot is marginally affected by H_2O dilution when $\xi_a = 1.5$.

C. Chemical effects of water vapor diluent

The chemical effects of H_2O vapor dilution on autoignition and detonation development of stoichiometric n-C_7H_{16}/air mixtures due to the ignition spot are investigated in this section. Similar to the
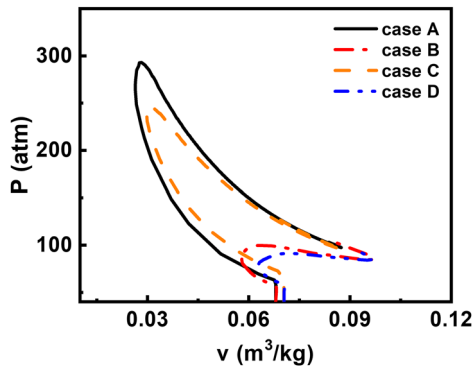
FIG. 12. P–v (pressure vs specific volume) diagram of the fluid particle initially at $r = r_0$ in cases A to D.

0D calculations in Sec. III, numerical experiments with hypothetical H_2O species, i.e., FH_2O and TH_2O, are conducted. The reader is reminded that the former denotes a chemically inert species (not the reactant or third body), while the latter acts as a third body only. Figure 13 shows the autoignition modes of stoichiometric n-C_7H_{16}/air mixtures with different diluent (H_2O, FH_2O, or TH_2O) mole fractions due to the temperature gradient in the ignition spot. The spot radius is $r_0 = 3.5$ mm. The curve of H_2O is the same as the curve in Fig. 6. For the curves with FH_2O and TH_2O, three categories of autoignition modes are present for small and intermediate dilute mole fractions. The detonation development curves are all mirrored C-shaped. It is noted that the upper limit $\xi_{a,u}$ of FH_2O is obviously higher than those of real H_2O as well as TH_2O. However, the chemical effects of water vapor diluents do not affect the lower limits $\xi_{a,l}$. This is because the average speed of the autoignition front propagating within the ignition spot is faster for a lower ξ_a. Besides, the critical mole fraction of FH_2O is about 0.16, which is higher than the counterparts with H_2O and TH_2O. This indicates that the chemical effects, especially the third body effect, are important in suppressing detonation development for the investigated ignition spot size.
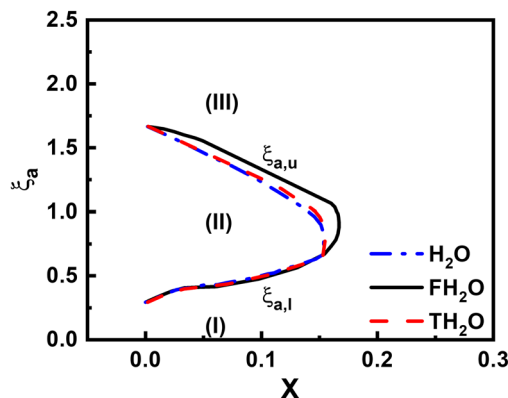
FIG. 13. Autoignition modes of stoichiometric n-C_7H_{16}/air/FH_2O and n-C_7H_{16}/air/TH_2O mixtures with the H_2O mole fraction. Hotspot size is $r_0 = 3.5$ mm. Three categories are as follows: (I) supersonic deflagrative wave, (II) detonative wave, and (III) subsonic deflagrative wave.

This is consistent with the observations from the 0D simulations in Sec. III.

Figure 14 further shows the P–v diagram of the particle initially at the right edge of the hotspot ($r = r_0 = 3.5$ mm) and the reaction front propagation speed of stoichiometric n-C_7H_{16}/air mixtures with different diluents. The mole fractions of various diluents (i.e., H_2O, FH_2O, and TH_2O) are fixed to be 0.1. The results of cases C and D tabulated in Table I act as the reference for each value of ξ_a. For $\xi_a = 0.5$, all autoignition modes correspond to detonation development, while for $\xi_a = 1.5$, they correspond to subsonic reaction front propagation (see Fig. 13). Seen from Fig. 14(a), the curves almost overlap for the corresponding ξ_a. This indicates that evolutions of the thermal states of the particle are almost unaffected by the chemical effects of water dilution. It is seen from Fig. 14(b) that the reaction front propagation speeds are very close for $\xi_a = 0.5$. This also confirms that the chemical effects of water dilution are weak for a lower ξ_a. When ξ_a is increased to 1.5, similar tendency is found within the hotspot, but the reaction front propagation speed is considerably affected. After the flame acceleration caused by thermal explosion around the edge of the hotspot, the supersonic reaction front speeds in the mixtures with FH_2O and TH_2O approach the C–J detonation speed. However, the corresponding normalized maximum pressure P_{max}/P_e (≈ 1.86 for FH_2O and 1.78 for TH_2O) is lower than that of a typical detonation wave (>2.0). Then, the sudden increase in the propagation speed within a short time occurs, caused by multiple
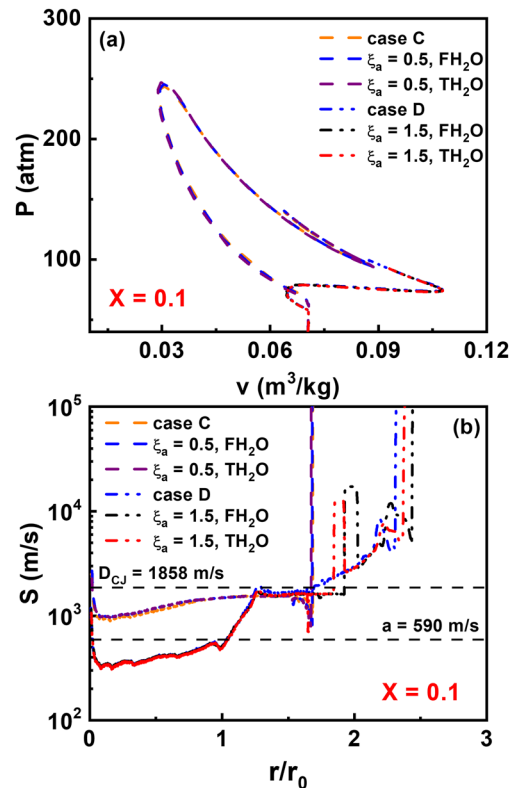
FIG. 14. Change in thermal state and propagation speed of stoichiometric n-C_7H_{16}/air mixtures: (a) P–v diagram of the fluid particle and (b) reaction front propagation speed.
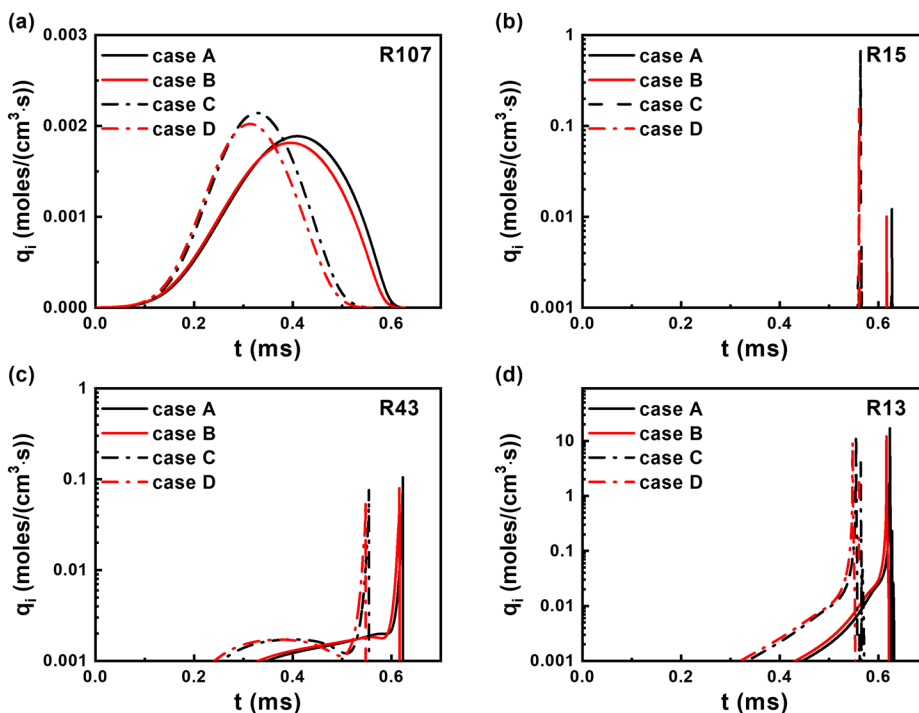
FIG. 15. Time history of the rate of progress variable q_i for selected elementary reactions at a static point near the left boundary ($r = r_0/100 = 0.035\,\text{mm}$). (a) R107, (b) R15, (c) R43, and (d) R13.

peaks of heat release rate. Such phenomena have not been observed in case D. This is because the total heat release decreases (see Fig. 5), and meanwhile, only single peak of heat release rate exists before autoignition happens near the right boundary [i.e., line No. 1 to No. 5 of Fig. 9(c)] when the real H_2O is added. This indicates that the chemical effects become important for thermal explosion in the end gas for $\xi_a = 1.5$.

Figure 15 shows the time history of the rate of progress variable q_i for the selected elementary reactions (R107, R15, R43, and R13) at a static probe point near the left boundary (at $r = 0.035\,\text{mm}$) for cases A–D. q_i is given by the difference of the forward and reverse rates. These four elementary reactions are selected based on the sensitivity analysis shown in Fig. 6. As mentioned previously before, R107 and R43 are relevant to the combustion of n-C_7H_{16}. R13 is important for the low-carbon oxidation; in addition, H_2O acts as a product here. R15 is very effective in producing OH radicals, and H_2O also acts as a third body here. Except for R15, similar distributions and maximum values of q_i for R107, R43, and R13 are observed for cases A–D. In other words, they are little affected by the H_2O molar fraction and normalized temperature gradient. In terms of R15, the maximum value of q_{15} (i.e., q_i for R15) with H_2O dilution is at least one order greater than that without H_2O dilution for the corresponding normalized temperature gradient. Therefore, it is confirmed that R15 is the crucial elementary reaction during 1D autoignition with H_2O dilution. This is also consistent with the results for CH_4 mixtures.[67]

D. Autoignition mode under various conditions

Up to this point, the equivalence ratio (ϕ) and ignition spot size (r_0) are fixed to be 1.0 mm and 3.5 mm, respectively. It has been shown that variations of either of them would have significant effects on autoignition and detonation characteristics of H_2O diluted n-C_7H_{16}/air mixtures.[34] Figure 16 summarizes the autoignition modes of n-C_7H_{16}/air/H_2O mixtures due to the temperature non-uniformity in the ignition spot under different equivalence ratios ϕ. Six different ϕ are considered. The spot radius is fixed to be $r_0 = 3.5$ mm. Obviously, all detonation development curves are mirrored C-shaped. It is seen from Fig. 16 that, compared with stoichiometric and furl-rich mixtures, for fuel-leaner mixtures, its upper limit $\xi_{a,u}$ becomes smaller, and the lower limit $\xi_{a,l}$ is larger,
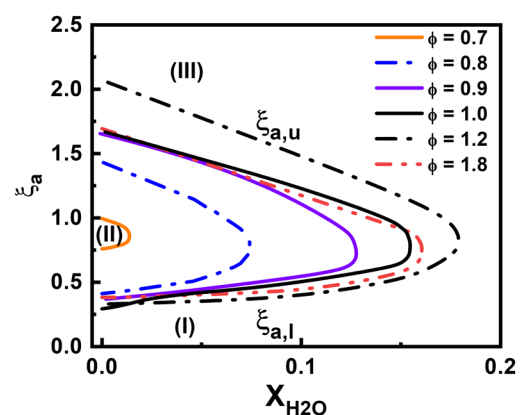
FIG. 16. Autoignition mode under different equivalence ratios. $r_0 = 3.5$ mm and $T_{i,0} = 1000$ K. Three categories are as follows: (I) supersonic deflagrative wave, (II) detonative wave, and (III) subsonic deflagrative wave.

which leads to a more compact curve in the $\xi_a - X_{H_2O}$ diagram and hence the shrinking range of ξ_a for detonation devolvement. In addition, the corresponding critical H_2O mole fraction is also decreased. Therefore, one can conclude that water vapor addition in fuel-lean mixtures is more advantageous to inhibit detonation development from localized thermal non-uniformity. This is also observed by Dai et al.[34]

Furthermore, Fig. 17 shows the normalized maximum pressure, P_{max}/P_e, vs normalized excitation time, τ_e/τ_e^0, corresponding to the conditions presented in Fig. 16. The normalized temperature gradient is $\xi_a = 1.0$. Fuel-lean ($\phi = 0.8$) and stoichiometric mixtures are chosen to further show the differences. In general, P_{max}/P_e decreases monotonically when the normalized excitation time increases. It is also seen that P_{max}/P_e corresponding to $\phi = 0.8$ is obviously smaller when the normalized excitation time is fixed. This indicates that the chemistry–acoustics interaction is weakened under fuel-lean conditions.

All above results are obtained with a fixed size of the ignition spot, i.e., $r_0 = 3.5$ mm. The effects of ignition spot size on detonation limits are illustrated in Fig. 18. It is shown the autoignition modes of stoichiometric n-C_7H_{16}/air mixtures in the $\xi_a - \varepsilon$ diagram in terms of varying ignition spot sizes. Note that the normalized acoustic time scale ε is proportional to r_0 [see Eq. (11)]. A stoichiometric mixture with a constant H_2O mole fraction is considered, i.e., diluted mixture ($X_{H_2O} = 0.13$) with $T_{i,0} = 1000$ K. The one (undiluted mixture with $T_{i,0} = 1000$ K) from Ref. 34 is added for reference. For a fixed ε, the corresponding r_0 of the diluted mixture is larger for that of the undiluted mixture. This is mainly caused by the larger extinction time with water vapor addition. It is found from Fig. 18 that the detonation development curves are all C-shaped. For the range of r_0 investigated here, the critical ε corresponding to the right end of each curve is considerably different. The maximum ε of detonation limit for the undiluted mixture is 22 at $r_0 = 5$ mm, whereas it is reduced to a smaller one (i.e., $\varepsilon \approx 12$ at $r_0 = 8$ mm) for the diluted one. Besides, estimated from Fig. 18, the minimum ignition spot size required by detonation development (i.e., the left end of each curve) changes from $r_0 \approx 1.2$ mm in the undiluted mixture to $r_0 \approx 2.9$ mm in the diluted mixture. These indicate that water vapor
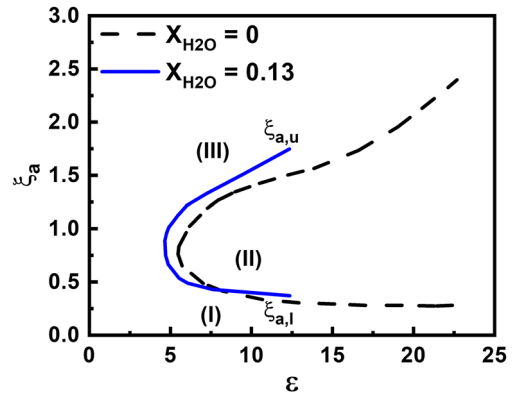
FIG. 18. Autoignition mode of stoichiometric mixtures under different ignition spot sizes in the $\xi_a - \varepsilon$ diagram. $T_{i,0} = 1,000$ K. Dashed line: $X_{H_2O} = 0$; Solid line: $X_{H_2O} = 0.13$. The dashed line is from Ref. 34. Three categories are as follows: (I) supersonic deflagrative wave, (II) detonative wave, and (III) subsonic deflagrative wave.

dilution can appreciably affect the detonation limits of n-C_7H_{16}/air mixtures.

Figure 19 shows the change in normalized maximum pressure P_{max}/P_e with the normalized temperature gradient ξ_a for n-C_7H_{16}/air/H_2O mixtures under different hotspot sizes. The H_2O mole fraction is $X_{H_2O} = 0.13$. One can see that, for a fixed r_0, a maximum value of P_{max}/P_e exists around $\xi_a \approx 1$. Furthermore, with increased r_0, P_{max}/P_e also increases, which indicates that the interaction between the reaction wave and the pressure wave is strengthened. This may be caused by the higher propensity for them to get coupled with each other inside the hotspot. Besides, the maximum value of P_{max}/P_e for $r_0 = 2$ mm is relatively small, as no detonation occurs. It is noted that P_{max}/P_e is relatively high when ξ_a is greater than 2 for $r_0 = 8$ mm. However, it is still obviously lower than the typical value of a detonation wave.
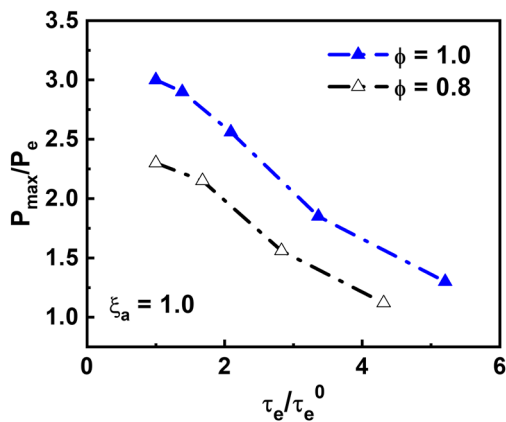
FIG. 17. Change in normalized maximum pressure with normalized excitation time. $r_0 = 3.5$ mm and $T_{i,0} = 1000$ K.
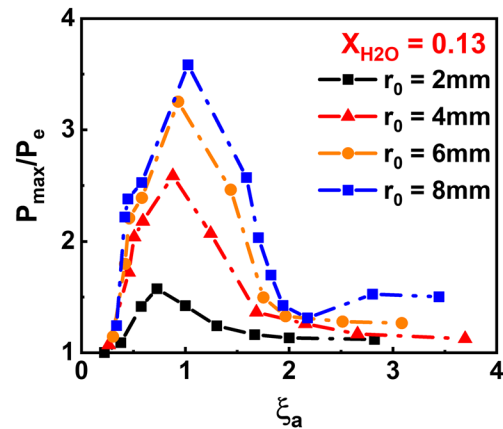
FIG. 19. Change in normalized maximum pressure with the normalized temperature gradient in stoichiometric mixtures with different hotspot sizes. $X_{H_2O} = 0.13$.

V. CONCLUSION

The effects of water vapor dilution on autoignition and detonation development induced by temperature gradients in n-C_7H_{16}/air mixtures are numerically studied in this work. Zero-dimensional homogeneous ignition under the constant-volume condition is first calculated. It is found that the increased H_2O mole fraction has a negligible influence on the NTC temperature range for the stoichiometric mixture. However, the NTC effect is weakened with H_2O dilution. Besides, excitation time increases, whereas the total heat release decreases with the H_2O mole fraction. It is also seen that the third body effect of the H_2O vapor diluent considerably influences the critical temperature gradient.

Autoignition front propagation from an ignition spot in n-C_7H_{16}/air/H_2O mixtures is analyzed based on one-dimensional simulations. The performance of H_2O dilution, the typical autoignition process, the underlying chemical effects, and the influences of various initial conditions are discussed. One can see from the detonation peninsula, i.e., $\xi_a - X_{H_2O}$ diagram, that three autoignition modes can be identified, i.e., supersonic deflagrative wave, detonative wave, and subsonic deflagrative wave. It is also noted that H_2O dilution has a slightly better performance in detonation suppression compared with CO_2 dilution. Besides, the chemical effects, especially the third body effect, are important in suppressing detonation development. It is also shown that $2OH + M <=> H_2O_2 + M$ is the crucial elementary reaction during 1D autoignition with H_2O dilution. Moreover, it is observed that the water vapor diluted n-C_7H_{16}/air mixtures with the fuel-lean condition have less propensity for detonation development from localized thermal non-uniformity.

ACKNOWLEDGMENTS

DATA AVAILABILITY

The data that support the findings of this study are available from the corresponding author upon reasonable request.

REFERENCES

[1]Z. Wang, H. Liu, and R. D. Reitz, "Knocking combustion in spark-ignition engines," Prog. Energy Combust. Sci. **61**, 78 (2017).

[2]K. P. Grogan, S. Scott Goldsborough, and M. Ihme, "Ignition regimes in rapid compression machines," Combust. Flame **162**, 3071 (2015).

[3]J. Rudloff, J.-M. Zaccardi, S. Richard, and J. M. Anderlohr, "Analysis of pre-ignition in highly charged SI engines: Emphasis on the auto-ignition mode," Proc. Combust. Inst. **34**, 2959 (2013).

[4]C. Dahnz and U. Spicher, "Irregular combustion in supercharged spark ignition engines - pre-ignition and other phenomena," Int. J. Eng. Res. **11**, 485 (2010).

[5]N. Peters, B. Kerschgens, and G. Paczko, "Super-Knock prediction using a refined theory of turbulence," SAE Int. J. Engines **6**, 953 (2013).

[6]M. D. Kurtz and J. D. Regele, "Acoustic timescale characterisation of a one-dimensional model hot spot," Combust. Theory Modell. **18**, 532 (2014).

[7]H. Wei, X. Zhang, H. Zeng, R. Deiterding, J. Pan, and L. Zhou, "Mechanism of end-gas autoignition induced by flame-pressure interactions in confined space," Phys. Fluids **31**, 076106 (2019).

[8]Z. Wang, H. Liu, T. Song, Y. Qi, X. He, S. Shuai, and J. Wang, "Relationship between super-knock and pre-ignition," Int. J. Eng. Res. **16**, 166 (2015).

[9]Z. Wang, Y. Qi, X. He, J. Wang, S. Shuai, and C. K. Law, "Analysis of pre-ignition to super-knock: Hotspot-induced deflagration to detonation," Fuel **144**, 222 (2015).

[10]M. Reynaud, F. Virot, and A. Chinnayya, "A computational study of the interaction of gaseous detonations with a compressible layer," Phys. Fluids **29**, 056101 (2017).

[11]Y. Liu, W. Zhou, Y. Yang, Z. Liu, and J. Wang, "Numerical study on the instabilities in H_2-air rotating detonation engines," Phys. Fluids **30**, 046106 (2018).

[12]Y. Fang, Y. Zhang, X. Deng, and H. Teng, "Structure of wedge-induced oblique detonation in acetylene-oxygen-argon mixtures," Phys. Fluids **31**, 026108 (2019).

[13]Y.Zeldovich, "Regime classification of an exothermic reaction with nonuniform initial conditions," Combust. Flame **39**, 211 (1980).

[14]D. Bradley, C. Morley, X. Gu, and D. Emerson, "Amplified pressure waves during autoignition: Relevance to CAI engines," SAE Trans. **111**, 2679–2690 (2002).

[15]X. J. Gu, D. R. Emerson, and D. Bradley, "Modes of reaction front propagation from hot spots," Combust. Flame **133**, 63 (2003).

[16]D. Bradley and G. T. Kalghatgi, "Influence of autoignition delay time characteristics of different fuels on pressure waves and knock in reciprocating engines," Combust. Flame **156**, 2307 (2009).

[17]D. Bradley, "Autoignitions and detonations in engines and ducts," Philos. Trans. R. Soc., A **370**, 689 (2012).

[18]G. T. Kalghatgi and D. Bradley, "Pre-ignition and 'super-knock' in turbocharged spark-ignition engines," Int. J. Eng. Res. **13**, 399 (2012).

[19]G. Kalghatgi, "Knock onset, knock intensity, superknock and preignition in spark ignition engines," Int. J. Eng. Res. **19**, 7 (2018).

[20]L. Bates, D. Bradley, G. Paczko, and N. Peters, "Engine hot spots: Modes of autoignition and reaction propagation," Combust. Flame **166**, 80 (2016).

[21]L. Bates and D. Bradley, "Deflagrative, auto-ignitive, and detonative propagation regimes in engines," Combust. Flame **175**, 118 (2017).

[22]L. Bates, D. Bradley, I. Gorbatenko, and A. S. Tomlin, "Computation of methane/air ignition delay and excitation times, using comprehensive and reduced chemical mechanisms and their relevance in engine autoignition," Combust. Flame **185**, 105 (2017).

[23]J. Pan, S. Dong, H. Wei, T. Li, G. Shu, and L. Zhou, "Temperature gradient induced detonation development inside and outside a hotspot for different fuels," Combust. Flame **205**, 269 (2019).

[24]Y. Gao, P. Dai, and Z. Chen, "Numerical studies on autoignition and detonation development from a hot spot in hydrogen/air mixtures," Combust. Theory Modell. **24**, 245 (2019).

[25]J. Pan, H. Wei, G. Shu, Z. Chen, and P. Zhao, "The role of low temperature chemistry in combustion mode development under elevated pressures," Combust. Flame **174**, 179 (2016).

[26]J. Pan, H. Wei, G. Shu, and R. Chen, "Effect of pressure wave disturbance on auto-ignition mode transition and knocking intensity under enclosed conditions," Combust. Flame **185**, 63 (2017).

[27]H. Terashima and M. Koshi, "Mechanisms of strong pressure wave generation in end-gas autoignition during knocking combustion," Combust. Flame **162**, 1944 (2015).

[28]H. Terashima, A. Matsugi, and M. Koshi, "Origin and reactivity of hot-spots in end-gas autoignition with effects of negative temperature coefficients: Relevance to pressure wave developments," Combust. Flame **184**, 324 (2017).

[29]H. Terashima, A. Matsugi, and M. Koshi, "End-gas autoignition behaviors under pressure wave disturbance," Combust. Flame **203**, 204 (2019).

[30]P. Dai, Z. Chen, S. Chen, and Y. Ju, "Numerical experiments on reaction front propagation in n-heptane/air mixture with temperature gradient," Proc. Combust. Inst. **35**, 3045 (2015).

[31]P. Dai and Z. Chen, "Supersonic reaction front propagation initiated by a hot spot in n -heptane/air mixture with multistage ignition," Combust. Flame **162**, 4183 (2015).

[32]P. Dai and Z. Chen, "Effects of NOx addition on autoignition and detonation development in DME/air under engine-relevant conditions," Proc. Combust. Inst. **37**, 4813 (2019).

[33]P. Dai, C. Qi, and Z. Chen, "Effects of initial temperature on autoignition and detonation development in dimethyl ether/air mixtures with temperature gradient," Proc. Combust. Inst. **36**, 3643 (2017).

[34]P. Dai, Z. Chen, and X. Gan, "Autoignition and detonation development induced by a hot spot in fuel-lean and CO_2 diluted n-heptane/air mixtures," Combust. Flame **201**, 208 (2019).

[35]H. Yu and Z. Chen, "End-gas autoignition and detonation development in a closed chamber," Combust. Flame **162**, 4102 (2015).

[36]H. Yu, C. Qi, and Z. Chen, "Effects of flame propagation speed and chamber size on end-gas autoignition," Proc. Combust. Inst. **36**, 3533 (2017).

[37]J. Pan, G. Shu, P. Zhao, H. Wei, and Z. Chen, "Interactions of flame propagation, auto-ignition and pressure wave during knocking combustion," Combust. Flame **164**, 319 (2016).

[38]M. B. Luong, G. H. Yu, T. Lu, S. H. Chung, and C. S. Yoo, "Direct numerical simulations of ignition of a lean n-heptane/air mixture with temperature and composition inhomogeneities relevant to HCCI and SCCI combustion," Combust. Flame **162**, 4566 (2015).

[39]M. B. Luong, S. Desai, F. E. H. Pérez, R. Sankaran, B. Johansson, and H. G. Im, "A statistical analysis of developing knock intensity in a mixture with temperature inhomogeneities," Proc. Combust. Inst. (2020).

[40]M. B. Luong, F. E. Hernández Pérez, and H. G. Im, "Prediction of ignition modes of NTC-fuel/air mixtures with temperature and concentration fluctuations," Combust. Flame **213**, 382 (2020).

[41]H. G. Im, P. Pal, M. S. Wooldridge, and A. B. Mansfield, "A regime diagram for autoignition of homogeneous reactant mixtures with turbulent velocity and temperature fluctuations," Combust. Sci. Technol. **187**, 1263 (2015).

[42]F. Hoppe, M. Thewes, H. Baumgarten, and J. Dohmen, "Water injection for gasoline engines: Potentials, challenges, and solutions," Int. J. Eng. Res. **17**, 86 (2016).

[43]A. Li, Z. Zheng, and T. Peng, "Effect of water injection on the knock, combustion, and emissions of a direct injection gasoline engine," Fuel **268**, 117376 (2020).

[44]S. Zhu, B. Hu, S. Akehurst, C. Copeland, A. Lewis, H. Yuan, I. Kennedy, J. Bernards, and C. Branney, "A review of water injection applied on the internal combustion engine," Energy Convers. Manage. **184**, 139 (2019).

[45]J. Harrington, "Water addition to gasoline–effect on combustion, emissions, performance, and knock," SAE Trans. **91**, 1226–1251 (1982).

[46]J. Fitton and R. Nates, "Knock erosion in spark-ignition engines," SAE Trans. **105**, 2318–2326 (1996).

[47]H. Özcan and M. S. Söylemez, "Experimental investigation of the effects of water addition on the exhaust emissions of a naturally aspirated, liquefied-petroleum-gas-fueled engine," Energy Fuels **19**, 1468 (2005).

[48]A. Boretti, "Water injection in directly injected turbocharged spark ignition engines," Appl. Therm. Eng. **52**, 62 (2013).

[49]A. Iacobacci, L. Marchitto, and G. Valentino, "Water injection to enhance performance and emissions of a turbocharged gasoline engine under high load condition," SAE Int. J. Engines **10**, 928 (2017).

[50]Y. Zhuang, Q. Li, P. Dai, and H. Zhang, "Autoignition and detonation characteristics of n-heptane/air mixture with water droplets," Fuel **266**, 117077 (2020).

[51]R. J. Kee, F. M. Rupley, and J. a. Miller, "CHEMKIN-II: A FORTRAN chemical kinetics package for the analysis of gas phase chemical kinetics," Report SAND89-8009B, Sandia National Laboratories, Livermore, CA, USA, 1989.

[52]R. Kee, J. Grcar, M. Smooke, J. Miller, and E. Meeks, "PREMIX : A FORTRAN program for modeling steady laminar one-dimensional," SAND85-8249, Sandia National Laboratories, Livermore, CA, USA, 1985.

[53]Z. Chen, *Studies on the Initiation, Propagation, and Extinction of Premixed Flames* (Princeton University, Princeton, USA, 2009).

[54]Z. Chen, M. P. Burke, and Y. Ju, "Effects of Lewis number and ignition energy on the determination of laminar flame speed using propagating spherical flames," Proc. Combust. Inst. **32**, 1253 (2009).

[55]Z. Chen, "Effects of radiation and compression on propagating spherical flames of methane/air mixtures near the lean flammability limit," Combust. Flame **157**, 2267 (2010).

[56]S. Liu, J. C. Hewson, J. H. Chen, and H. Pitsch, "Effects of strain rate on high-pressure nonpremixed n-heptane autoignition in counterflow," Combust. Flame **137**, 320 (2004).

[57]M. Sun and K. Takayama, "Conservative smoothing on an adaptive quadrilateral grid," J. Comput. Phys. **150**, 143 (1999).

[58]W. Zhang, X. Gou, and Z. Chen, "Effects of water vapor dilution on the minimum ignition energy of methane, n -butane and n -decane at normal and reduced pressures," Fuel **187**, 111 (2017).

[59]J. O. Olsson and L. L. Andersson, "Sensitivity analysis based on an efficient brute-force method, applied to an experimental CH_4O_2 premixed laminar flame," Combust. Flame **67**, 99 (1987).

[60]R. K. Maurya and N. Akhil, "Development of a new reduced hydrogen combustion mechanism with NOx and parametric study of hydrogen HCCI combustion using stochastic reactor model," Energy Convers. Manage. **132**, 65 (2017).

[61]Y. Zhang, J. Fu, J. Shu, M. Xie, J. Liu, T. Jiang, Z. Peng, and B. Deng, "Numerical study on auto-ignition characteristics of hydrogen-enriched methane under engine-relevant conditions," Energy Convers. Manage. **200**, 112092 (2019).

[62]T. Poinsot and D. Veynante, *Theoretical and Numerical Combustion* (RT Edwards, Inc., 2005).

[63]C. A. Z. Towery, A. Y. Poludnenko, and P. E. Hamlington, "Detonation initiation by compressible turbulence thermodynamic fluctuations," Combust. Flame **213**, 172 (2020).

[64]H. D. Ng and J. H. S. Lee, "Direct initiation of detonation with a multi-step reaction scheme," J. Fluid Mech. **476**, 179 (2003).

[65]C. Qi and Z. Chen, "Effects of temperature perturbation on direct detonation initiation," Proc. Combust. Inst. **36**, 2743 (2017).

[66]R. Zhou and J.-P. Wang, "Numerical investigation of flow particle paths and thermodynamic performance of continuously rotating detonation engines," Combust. Flame **159**, 3632 (2012).

[67]E. A. Tingas, D. C. Kyritsis, and D. A. Goussis, "Algorithmic determination of the mechanism through which H_2O-dilution affects autoignition dynamics and NO formation in CH_4/air mixtures," Fuel **183**, 90 (2016).